

Effective Tight-Binding Hamiltonian for Transition Metal Dichalcogenides

Final Year Project Report

03 April 2017

Alden Pong Ming Xuan
Department of Physics, National University of Singapore

Contents

| | | |
|----------|--|-----------|
| 1 | Introduction | 3 |
| 1.1 | Transition Metal Dichalcogenides | 3 |
| 1.2 | Tight-Binding Model | 3 |
| 1.3 | Objectives | 4 |
| 2 | Effective Tight-Binding Hamiltonian for TMDs | 4 |
| 2.1 | Theoretical Background I | 4 |
| 2.1.1 | Bloch function | 4 |
| 2.1.2 | Linear combination of atomic orbitals (LCAO) | 5 |
| 2.1.3 | Tight Binding Model | 6 |
| 2.2 | Results I: Implementation of Tight-Binding | 10 |
| 2.2.1 | A First Approximation | 13 |
| 2.2.2 | Refinement of Results | 16 |
| 3 | Charge Density Waves in metallic TMDs: Case Study of NbSe₂ | 17 |
| 3.1 | Theoretical Background II: | 17 |
| 3.1.1 | Charge Density Waves (CDW) | 17 |
| 3.1.2 | Lindhard response function and Fermi Surface Nesting (FSN) | 21 |
| 3.1.3 | Experimental findings for NbSe ₂ . FSN vs EPC | 21 |
| 3.1.4 | Electron-Phonon Coupling (EPC) | 22 |
| 3.2 | Computation of the EPC matrix $g_{kn,k'n'}^\sigma$ | 26 |
| 4 | Conclusion | 28 |

1 Introduction

1.1 Transition Metal Dichalcogenides

Transition Metal Dichalcogenides(TMDs) is a class of materials with chemical formula MX_2 where M is a transition metal and X is a chalcogen. They typically exist in two lattice types in 2-Dimensions, Trigonal Prismatic and Trigonal Antiprismatic (rhombohedral). A specific TMD would favour one structure over the other for thermodynamic stability. There are a total of 3 layers of atoms in each monolayer, in the form X-M-X. Each layer by itself is arranged in a hexagonal 2-Dimensional lattice. The bulk form consists of stacks of these monolayers held together by weak Van der Waals forces. The X layers are inert, with no dangling bonds on the X atoms, allowing it to be stable in 2D.

Going from bulk to monolayer causes changes in electronic band structure. In some cases such as MoS_2 , indirect bandgaps become direct bandgaps[1, 9], making it useful for efficient optical applications due to conservation of momentum. MoS_2 has been of particular interest in part because it is cheap and occurs naturally. Monolayer MoS_2 has proven to be potentially useful as robust, flexible electronics for its semiconducting properties[1, 9](lacking in the well-studied Graphene that does not possess a bandgap). Digital electronics improve by getting smaller and smaller transistors so that more can be squeezed into a single device to maximize processing speed and power, making 2-D semiconductors particularly attractive as a working material. Some other uses where MoS_2 has shown potential usefulness include molecular sensing (owed to significant resistivity change with introduction of slight impurities due to 2-D nature), energy storage(as an electrode in Li-ion batteries) as well as a catalyst for the Hydrogen Evolution Reaction.[1]

In this project, we are interested in studying the metallic cases of 2D TMDs. In bulk form, some of these have been known to possess charge density wave(CDW) phases at low temperatures[2]. CDW phases are interesting to us as it is not yet a well understood phenomenon. By studying their presence in TMDs, we hope to have a better understanding of the fundamental physics that give rise to this phenomenon. The choice of 2D metallic TMDs as the material on which to study CDW is to take advantage of the simplicity of a 2D system in calculations. Specifically, we wish to compute the electron-phonon coupling matrix which is likely a key driver of the CDW phases. The choice of method to perform this calculation is the tight-binding model.

1.2 Tight-Binding Model

The tight-binding model was first developed as a possible form of first-principles calculations for systems with tightly bound electrons such that one can make use of the wavefunctions on isolated versions of the constituent atoms as a good approximation of the wavefunctions in the full crystal lattice. Difficulties arise, however, in the computation of some complicated integrals, particularly so back in the times when modern computers were not widely available to assist in calculations. In many cases, as with our application of it in this project, it is adapted for use as a semi-empirical method, by treating the complicated integrals, whose results are just numerical constants, as

fitting parameters to use to fit to other accessible sources of data such as from experiments. More details on its applications will be covered later in Section 2.1.3. As a semi-empirical method, one can thus expect to obtain results with accuracy and rigour between that of first principles calculations and fully empirical methods. The advantage of such a method is in retaining parts of the physical insights one would expect from first-principles calculations in the final form of the result while benefitting from the greater ease of computation in empirical methods.

The electron-phonon coupling matrix involves lattice distortions accounted for in the hamiltonian of a system and is, in general, not a simple quantity to calculate. To perform a full first-principles calculation from the full quantum mechanical hamiltonian would require a sizeable computation time. Yet, the need to better understand charge density waves in terms of fundamental physics suggests empirical models may not provide us with the insights we seek. We thus choose to use a semi-empirical model to generate an 'effective hamiltonian' for this purpose instead. The choice of tight-binding specifically is for its particular suitability for studying TMDs whose tightly bound outermost d orbitals on the transition metal atom are known to play a large role in their electronic properties. Besides the electron-phonon coupling matrix, we expect this effective tight-binding hamiltonian to be useful in helping us compute other quantities related to phenomena we seek a better physical understanding of that are similarly difficult to compute using first-principles calculations from the full quantum mechanical hamiltonian.

1.3 Objectives

The two main objectives/sections in this project are thus:

1. To develop an effective method to build tight-binding hamiltonians for transition metal dichalcogenides in general, and
2. To apply that method to the case of monolayer Niobium Diselenide, NbSe₂, in an attempt to calculate the its electron-phonon coupling matrix and gain insight into its charge density wave behaviour

2 Effective Tight-Binding Hamiltonian for TMDs

2.1 Theoretical Background I

2.1.1 Bloch function

Bloch's theorem states that the periodicity of crystals imply that the electronic wave function can be written as

$$\psi_{nk}(r) = \frac{1}{\sqrt{N}} e^{-ik \cdot r} u_{nk}(r) \quad (1)$$

where n denotes energy band while k specifies the wave vector k associated with that wave function. r denotes an arbitrary position and N is a normalization constant. Let

R represent the position of a unit cell. By symmetry of the crystal, ψ must be periodic in R . So we define $u_{nk}(r) = u_{nk}(r + R)$. With these conditions it can be seen that

$$\psi_{nk}(r + R) = \frac{1}{\sqrt{N}} e^{-ik \cdot (r+R)} u_{nk}(r + R) = e^{-ik \cdot R} \left(\frac{1}{\sqrt{N}} e^{-ik \cdot r} u_{nk}(r) \right) = e^{-ik \cdot R} \psi_{nk}(r)$$

Recognizing $e^{-ik \cdot r}$ as the translation operator in momentum representation, this means $\psi_{nk}(r + R)$ is obtained simply by translating $\psi_{nk}(r)$ to the lattice site R , giving the same wave function but centered at this new position. Hence, periodicity of the wave function is satisfied. $\psi_{nk}(r)$ can be interpreted physically as a plane wave $e^{-ik \cdot r}$ that is periodic in the crystal with unit cell position R , modulated periodically also with R by a periodic potential $u_{nk}(r)$.

2.1.2 Linear combination of atomic orbitals (LCAO)

Since the tight-binding model relies on approximating tightly bound electrons with wave-functions very similar to that of isolated atoms, the linear combination of atomic orbitals is a very natural choice of basis. Here, we present the construction of the LCAO basis set we will use in the tight-binding model.

To begin, we assume that the full wave function can be written in terms of the wave functions of atomic orbitals (wave functions of isolated atoms). Start with a trial wave function:

$$|\chi_{\alpha,i,k}\rangle = \frac{1}{\sqrt{N_{\alpha,i}}} \sum_R e^{ik \cdot R} |\phi_{\alpha,i}(R)\rangle \quad (2)$$

$|\phi_{\alpha,i}(R)\rangle$ is an atomic orbital, indexed by orbital i on atom α in a multi-atom basis. $N_{\alpha,i}$ is the number of unit cells that make up the crystal. The form of this equation already follows very closely the Bloch form Eq. (1). Comparing, we know that $\phi_{\alpha,i}(R) \sim u_{nk}(r)$, so as long as $\phi_{\alpha,i}(R)$ has the periodicity of the crystal, Bloch's theorem is satisfied. Projecting onto position basis r gives

$$\chi_{\alpha,i,k}(r) = \frac{1}{\sqrt{N_{\alpha,i}}} \sum_R e^{ik \cdot R} \phi_{\alpha,i}(r - u_{\alpha} - R)$$

u_{α} is used to give position of atom α within the unit cell. $\phi_{\alpha,i}(r - u_{\alpha} - R)$ obeys Bloch's theorem such that $\phi_{\alpha,i}(r - u_{\alpha} - R + T) = e^{-ik \cdot T} \phi_{\alpha,i}(r - u_{\alpha} - R)$ since the same atomic orbital on the same basis atom in any unit cell should be the same. Then,

$$\begin{aligned} \chi_{\alpha,i,k}(r + T) &= \frac{1}{\sqrt{N_{\alpha,i}}} \sum_R e^{ik \cdot R} \phi_{\alpha,i}(r - u_{\alpha} - R + T) \\ &= e^{-ik \cdot T} \frac{1}{\sqrt{N_{\alpha,i}}} \sum_R e^{ik \cdot R} \phi_{\alpha,i}(r - u_{\alpha} - R) \\ &= e^{-ik \cdot T} \chi_{\alpha,i,k}(r) \end{aligned}$$

So the trial wave function satisfies Bloch's theorem. The final wave function can be written as a linear combination of these trial wavefunctions (a linear combination of

Bloch states is still a Bloch state):

$$|\psi_{nk}\rangle = \sum_{\beta j} b_{\beta j}^n(k) |\chi_{\beta j,k}\rangle \quad (3)$$

2.1.3 Tight Binding Model

In the tight-binding model, wave functions are assumed to be highly localized with atomic orbitals decaying exponentially away from the atom. As such the overlaps between ‘distant’ atoms may be assumed to be negligible and set to 0. The threshold of distance depends on the level of accuracy desired. Beginning with Time-Independent Schrodinger equation:

$$\begin{aligned} H |\psi_{nk}\rangle &= E |\psi_{nk}\rangle \\ \langle \chi_{\alpha i,k} | H |\psi_{nk}\rangle &= E \langle \chi_{\alpha i,k} | \psi_{nk}\rangle \\ \sum_{\beta j} b_{\beta j}^n(k) \langle \chi_{\alpha i,k} | H |\chi_{\beta j,k}\rangle &= E \sum_{\beta j} b_{\beta j}^n(k) \langle \chi_{\alpha i,k} | \chi_{\beta j,k}\rangle \\ \sum_{\beta,j} (\langle \chi_{\alpha i,k} | H |\chi_{\beta j,k}\rangle - E \langle \chi_{\alpha i,k} | \chi_{\beta j,k}\rangle) b_{\beta j}^n(k) &= 0 \end{aligned} \quad (4)$$

We then define:

- Orbital overlap matrix: $\mathbf{S} = \langle \chi_{\alpha i,k} | \chi_{\beta j,k}\rangle$
- Hoppings overlap matrix: $\mathbf{H} = \langle \chi_{\alpha i,k} | H |\chi_{\beta j,k}\rangle$
- Effective tight-binding hamiltonian column vector of coefficients: $\mathbf{b} = \{b_{\beta j}^n(k)\}$

Then $(\mathbf{H} - E\mathbf{S}) \cdot \mathbf{b} = 0$ Is just the usual eigenvalue problem. In general, the overlaps can contain complicated integrals. These are treated as constant parameters (classified in a table of parameters according to specific overlap orientations between specific orbital types in a paper by Slater and Koster[7]) to be used to do statistical fits of the resultant energy band equations to data from more accurate sources such as fully ab initio methods (eg. Density Functional Theory) or experiments. The differences will be used to determine if more refinements need to be added by considering more terms, namely, more neighbours or more orbitals. The end goal is to obtain an effective tight-binding hamilton which balances simplicity with accuracy of results desired. To see how this process works in practice, we look at a few simple examples.

Basic example. One atom, one orbital basis, nearest-neighbour only. For simplicity let us first consider the case of a monolayer TMD, taking into account only interactions between the d_{z^2} orbitals of the transition metal atoms. This may be pictured as a simple 2D hexagonal lattice with a metal atom at each lattice site as depicted in Fig. 1.

We first define three basis vectors of the hexagonal lattice for convenience:

$$a_1 = a(1, 0), a_2 = a(\frac{1}{2}, \frac{\sqrt{3}}{2}), a_3 = a(-\frac{1}{2}, \frac{\sqrt{3}}{2})$$

where a is the lattice constant.

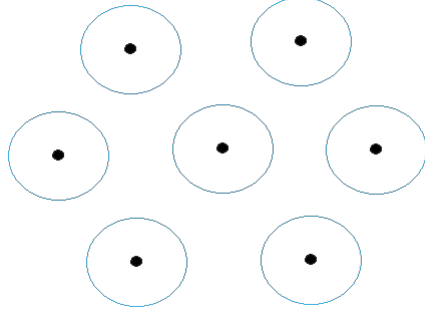


Figure 1: z-axis pointing into the plane. Black dots indicate metal atom sites, blue circles depict symmetry of d_{z^2} orbitals

The trial wave function in Eq. (2) may then be written simply as

$$|\chi_k\rangle = \frac{1}{\sqrt{N}} \sum_R e^{ik \cdot R} |\phi(R)\rangle$$

The eigenvalue equation Eq. (4) to be solved then looks like

$$(\langle \chi_k | H | \chi_k \rangle - E \langle \chi_k | \chi_k \rangle) b^n(k) = 0$$

Which simply gives

$$\langle \chi_k | H | \chi_k \rangle = E$$

Evaluation of $\langle \chi | H | \chi \rangle$ is as follows:

$$\begin{aligned} \langle \chi_k | H | \chi_k \rangle &= \frac{1}{N} \sum_{R, R'} e^{ik \cdot (R - R')} \langle \phi(R') | H | \phi(R) \rangle \\ &= \sum_R e^{ik \cdot R} \langle \phi(0) | H | \phi(R) \rangle \\ &= \sum_R e^{ik \cdot R} \int d\mathbf{r} \phi^*(0) H \phi(R) \end{aligned}$$

In this step, we use the translational symmetry of the crystal to know that the sum of overlaps with all lattice sites is the same regardless of which initial lattice site it is measured from. So the summation over one index, either R or R' , will simply multiply the sum of overlaps with all lattice sites by the number of initial lattice sites, which is equivalent to the number of unit cells, thus multiplying a factor N to cancel out the initial factor of $\frac{1}{N}$. This step is useful and important as N is infinite since we are considering an infinite crystal lattice. It is also universally applicable in all cases so it will be skipped in future examples.

Continuing on, for this example, we only consider nearest neighbour interactions. This means the overlap integrals between states located at sites beyond nearest-neighbours are assumed to be negligible and set to 0. Then,

$$\begin{aligned}
\langle \chi_k | H | \chi_k \rangle &= \sum_R e^{ik \cdot R} \int dr \phi^*(0) H \phi(R) \\
&= \sum_R e^{ik \cdot R} E_{dz2, dz2} \\
&= (e^{ik \cdot a_1} + e^{-ik \cdot a_1} + e^{ik \cdot a_2} + e^{-ik \cdot a_2} + e^{ik \cdot a_3} + e^{-ik \cdot a_3}) E_{dz2, dz2} \\
&= 2(\cos(k_x a) + \cos(\frac{\sqrt{3}}{2} k_y a + \frac{1}{2} k_x a) + \cos(\frac{\sqrt{3}}{2} k_y a - \frac{1}{2} k_x a)) E_{dz2, dz2}
\end{aligned}$$

The integral is rewritten as the constant $E_{dz2, dz2}$. The integrals over different R are known to be the same as the d_{z2} orbital is symmetric about the z-axis, and all the neighbours are indeed located in the same x-y plane about the z-axis. This constant may be further rewritten in terms of Slater-Koster parameters for better organization in more complex systems, but is unnecessary for this example. This constant can now be chosen to fit the Energy band obtained to other reference data.

A simple extension to improve the accuracy of fitting is to increase the number of neighbours taken into consideration. In this case, if we were to take the next-nearest neighbours, an additional set of terms would arise as follows:

$$\begin{aligned}
\langle \chi_k | H | \chi_k \rangle &= \sum_R e^{ik \cdot R} \int dr \phi^*(0) H \phi(R) \\
&= (e^{ik \cdot a_1} + e^{-ik \cdot a_1} + e^{ik \cdot a_2} + e^{-ik \cdot a_2} + e^{ik \cdot a_3} + e^{-ik \cdot a_3}) E_{dz2, dz2}[a] \\
&\quad + (e^{ik \cdot (a_1+a_2)} + e^{-ik \cdot (a_1+a_2)} + e^{ik \cdot (a_2+a_3)} \\
&\quad + e^{-ik \cdot (a_2+a_3)} + e^{ik \cdot (a_3-a_1)} + e^{-ik \cdot (a_3-a_1)}) E_{dz2, dz2}[\sqrt{3}a]
\end{aligned}$$

Here, the constant parameters labeled by the distance between the overlapping orbitals to differentiate overlaps of the same type but over different distances.

Second example. Two atoms, one orbital basis, nearest-neighbour only. This second example will demonstrate a case where a matrix equation is obtained and must be diagonalized to obtain the eigenenergies. For this example, we look at graphene, considering only p_z orbital overlaps between nearest-neighbours. Graphene has a two-atom basis arranged in a hexagonal lattice. Let us label the two atoms as sublattice A and sublattice B and the vector going from A to B δ_1 .

Again, we first define three relevant vectors for convenience:

$$\begin{aligned}
\delta_1 &= a(0, \frac{1}{\sqrt{3}}) \\
\delta_2 &= -a_2 + \delta_1 = (-\frac{1}{2}, -\frac{1}{2\sqrt{3}}) \\
\delta_3 &= -a_3 + \delta_1 = (\frac{1}{2}, -\frac{1}{2\sqrt{3}})
\end{aligned}$$

These connect an atom in sublattice A to its three nearest neighbours.
The trial wavefunctions are then:

$$\chi_{A,k}(r) = \frac{1}{\sqrt{N_A}} \sum_R e^{ik \cdot R} \phi_{\alpha,i}(r - R)$$

$$\chi_{B,k}(r) = \frac{1}{\sqrt{N_B}} \sum_R e^{ik \cdot R} \phi_{\alpha,i}(r - \delta_1 - R)$$

The energy overlap matrix elements $\langle \chi_{\alpha,k} | H | \chi_{\beta,k} \rangle$ are then,

$$\begin{aligned} \langle \chi_{A,k} | H | \chi_{A,k} \rangle &= \sum_R e^{ik \cdot R} \int dr \phi_A^*(0) H \phi_A(R) \\ &= \int dr \phi_A^*(0) H \phi_A(0) \\ &= \epsilon_{AA} \end{aligned}$$

$$\begin{aligned} \langle \chi_{B,k} | H | \chi_{B,k} \rangle &= \sum_R e^{ik \cdot R} \int dr \phi_B^*(0) H \phi_B(R) \\ &= \int dr \phi_B^*(0) H \phi_B(0) \\ &= \epsilon_{BB} \end{aligned}$$

$$\begin{aligned} \langle \chi_{A,k} | H | \chi_{B,k} \rangle &= \sum_R e^{ik \cdot R} \int dr \phi_A^*(0) H \phi_B(R) \\ &= (e^{ik \cdot \delta_1} + e^{ik \cdot \delta_2} + e^{ik \cdot \delta_3}) E_{pz,pz} \end{aligned}$$

$$\begin{aligned} \langle \chi_{B,k} | H | \chi_{A,k} \rangle &= (\langle \chi_{A,k} | H | \chi_{B,k} \rangle)^\dagger \\ &= (e^{-ik \cdot \delta_1} + e^{-ik \cdot \delta_2} + e^{-ik \cdot \delta_3}) E_{pz,pz} \end{aligned}$$

Here we know $\epsilon_{AA} = \epsilon_{BB}$ since the onsite energies of the p_z orbitals of both carbon atoms in the basis should be the same. As above, the integrals over each nearest neighbour is the same as the p_z orbitals are symmetric about the z-axis.

And for the overlap matrix elements $\langle \chi_{\alpha,k} | \chi_{\beta,k} \rangle$,

$$\langle \chi_{A,k} | \chi_{A,k} \rangle = \langle \chi_{B,k} | \chi_{B,k} \rangle = 1$$

$$\begin{aligned}\langle \chi_{A,k} | \chi_{B,k} \rangle &= \sum_R e^{ik \cdot R} \int dr \phi_A^*(0) \phi_B(R) \\ &= (e^{ik \cdot \delta_1} + e^{ik \cdot \delta_2} + e^{ik \cdot \delta_3}) S_{pz,pz}\end{aligned}$$

$$\begin{aligned}\langle \chi_{B,k} | \chi_{A,k} \rangle &= \langle \chi_{A,k} | \chi_{B,k} \rangle^\dagger \\ &= (e^{-ik \cdot \delta_1} + e^{-ik \cdot \delta_2} + e^{-ik \cdot \delta_3}) S_{pz,pz}\end{aligned}$$

We then obtain the matrix eigenvalue equation:

$$\begin{pmatrix} \epsilon_{AA} & (e^{ik \cdot \delta_1} + e^{ik \cdot \delta_2} + e^{ik \cdot \delta_3}) E_{pz,pz} \\ (e^{-ik \cdot \delta_1} + e^{-ik \cdot \delta_2} + e^{-ik \cdot \delta_3}) E_{pz,pz} & \epsilon_{AA} \end{pmatrix} - \begin{pmatrix} E & (e^{ik \cdot \delta_1} + e^{ik \cdot \delta_2} + e^{ik \cdot \delta_3}) S_{pz,pz} E \\ (e^{-ik \cdot \delta_1} + e^{-ik \cdot \delta_2} + e^{-ik \cdot \delta_3}) S_{pz,pz} E & E \end{pmatrix} \begin{pmatrix} b_A^n(k) \\ b_B^n(k) \end{pmatrix} = 0$$

Simplifying, setting $f(k) = (e^{ik \cdot \delta_1} + e^{ik \cdot \delta_2} + e^{ik \cdot \delta_3})$;

$$\begin{pmatrix} \epsilon_{AA} - E & f(k)(E_{pz,pz} - S_{pz,pz} E) \\ f^*(k)(E_{pz,pz} - S_{pz,pz} E) & \epsilon_{AA} - E \end{pmatrix} \begin{pmatrix} b_A^n(k) \\ b_B^n(k) \end{pmatrix} = 0$$

$$\det \begin{vmatrix} \epsilon_{AA} - E & f(k)(E_{pz,pz} - S_{pz,pz} E) \\ f^*(k)(E_{pz,pz} - S_{pz,pz} E) & \epsilon_{AA} - E \end{vmatrix} = 0$$

Finally ,solving for this gives

$$E_{\pm} = \frac{\epsilon_{AA} \pm \sqrt{|f(k)|^2 E_{pz,pz}}}{1 \pm \sqrt{|f(k)|^2 S_{pz,pz}}}$$

2.2 Results I: Implementation of Tight-Binding

As observed above, the tight-binding method to be used is a relatively simple one. The approach is well-defined, and always the same regardless of the system under study. The only complications arise from the sheer number summation terms in each hamiltonian matrix if many neighbours are needed, or the sheer size of the matrix (dimensions $n \times n$ for a basis size of n orbitals) if many orbitals are needed. Following these will also be a large number of fitting parameters and thus a large parameter space to navigate in the fitting process, which is not easily done by hand.

The solution, therefore, is to implement a code that automatically carries out the calculations and outputs the hamiltonian of a specified crystal structure, neighbours and basis under consideration. Following which, an automated search for the best fit based

on energy band dispersion data provided to the code. This solution gives a straightforward way to easily reproduce an effective tight-binding hamiltonian for any solid state system of interest with minimal additional effort. The overall structure of the code is as follows(**note: all length computations are in units of the lattice constant a_0**).

The first segment builds the lattice, determines the overlaps and builds the hamiltonian in terms of the fitting parameters:

1. Specify crystal structure:
 - a) Primitive translation vectors $\{a_i\}$
 - b) Basis vectors within the unit cell $\{\delta_i\}$
 - c) Desired lattice size parameter L
2. Automated lattice construction by generating a list of coordinates with linear combinations of primitive translation vectors through $\sum_i m_i a_i$ with m taking values from L to $-L$.
3. Specify hoppings
 - a) Vectors between desired neighbours. (in terms of a_i and δ_j already defined)
 - b) Basis orbital set
 - c) Which basis orbitals are connected to which (i.e. which hoppings are have a non-zero overlap integral), and connected by which of the earlier defined hopping vectors (needed to calculate the exponential prefactors for each matrix element).
4. Automated construction of hamiltonian in terms of \vec{k} , with local energies ϵ and Slater Koster parameters V as fitting parameters.

This second segment maps out the brillouin zone to plot of band dispersions along high symmetry paths:

1. Specify high symmetry points in First Brillouin Zone
2. Specify order of points in which to traverse to define high symmetry path
3. Automatic generation of mapping tool converting any point along high symmetry path to coordinates in k-space.

The last segment fits the band dispersions to the reference data provided and outputs the result:

1. Specify reference energy band dispersion data. If provided as table of values, interpolation into continuous function is automated.
2. Specify which bands to fit to and band weights.

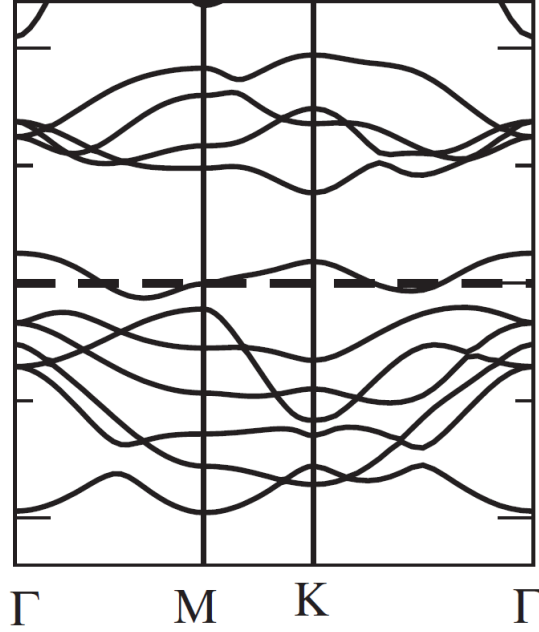


Figure 2: DFT band dispersion of monolayer NbSe₂. Dashed line indicates Fermi energy, set at 0 eV. Reproduced from [5].

3. Automated comparison of numerically diagonalized hamiltonian with reference energy bands and minimisation via the residue function $\sum_{\vec{k},n} w(n)(E_{code}^n(\vec{k}) - E_{reference}^n(\vec{k}))^2$ over high symmetry path. $w(n)$ is weight of the n -th band, E_{code} is the tight-binding energy and $E_{reference}$ is the reference energy bands.
 - a) (Optional) Variable density of sampling points
 - b) (Optional) Can use multiple random initial starting points in fitting parameter space to search for global minimum or starting a user-specified set of initial parameters
4. Automated generation of eigenvectors (corresponding to orbital compositions based on specified basis)

As a demonstration of the effectiveness of the code, as well as in the interest of the second part of the project, we implement the code using lattice parameters obtained from Moncton, Axe and DiSalvo [6], DFT band dispersion of monolayer NbSe₂ as calculated by Kumar and Ahluwalia[5]. The plot is shown here in Fig. 2.

2.2.1 A First Approximation

The computation and fitting procedure can take a sizeable computation time. Many different types and degrees of approximations are available and it is not initially obvious which details are important to keep while which are simply not worth the computational costs. It is thus desirable to make a few quick and crude fits first to eliminate factors less likely to be important and narrow down the number of different approximations to try with a detailed fit. With this, a few simple variations of the tight-binding approximations and fitting procedures were carried out for the case of monolayer, Trigonal Prismatic, Niobium Diselenide (2H-NbSe₂). By the end of the section, we hope to justify the choice of approximations and fitting methods with which we form our effective tight-binding hamiltonian.

Our preliminary fits are performed using only the five 4d orbitals of the transition metal atoms as the d bands are considerably isolated from the other bands according to DFT data and the orbital content of the conduction band that we are most interested in is expected to be very strongly dominated by d orbitals. The minimization is done by finding the minimum of the residue function defined as the difference of squares between the DFT data and the computed eigenvalues of our tight-binding hamiltonian, summed over 10 sampled k-points uniformly distributed along the $\Gamma - M - K - \Gamma$ high symmetry path. A random set of initial fitting parameters are generated with values between -1eV and 1eV as a starting point for the search for the minimum. For each of these cases, 10 fits with different initial fitting parameters are done and the result with the smallest residue is chosen and presented in this report. This is to minimize the variance in fitting quality that may arise from traps in local minimums in the residue function that are not the global minimum.

In the first case, we consider only nearest-neighbour overlaps in the orthogonal tight binding scheme. The fit is performed with equal weightage to the five known d bands and 0 weightage to all the others. We then use the same approximations and fitting procedures for the non-orthogonal approximation but feeding the parameter values obtained from the first fit as starting values for the search in hopes that we start closer to the true global minimum and thus have a better chance of finding it. Finally, this second calculation is performed again but using the randomized initial values instead of the results from the orthogonal case. The results are shown in Fig. 3.

From these 3 cases, it can be seen both from the quantitative value of the residue function as well as the qualitative appearance of the band diagram that including the S overlap matrix in the non-orthogonal approximation does not significantly improve the results. In contrast, the computation time taken as shown in Table 1 shows an increase by multiples of the orthogonal case when taking into account non-orthogonality.

In the next set of calculations, we repeat the same procedure but taking into account next-nearest-neighbour overlaps as well. The results are shown in Fig. 4.

The quantitative results are summarized in Table 1 for easy reference. As seen from the results in all 6 cases above, taking into account a non-orthogonal S overlap matrix makes no significant improvements to the fits obtained. As a result of the larger parameter space, the computational time is significantly longer and with this small preliminary

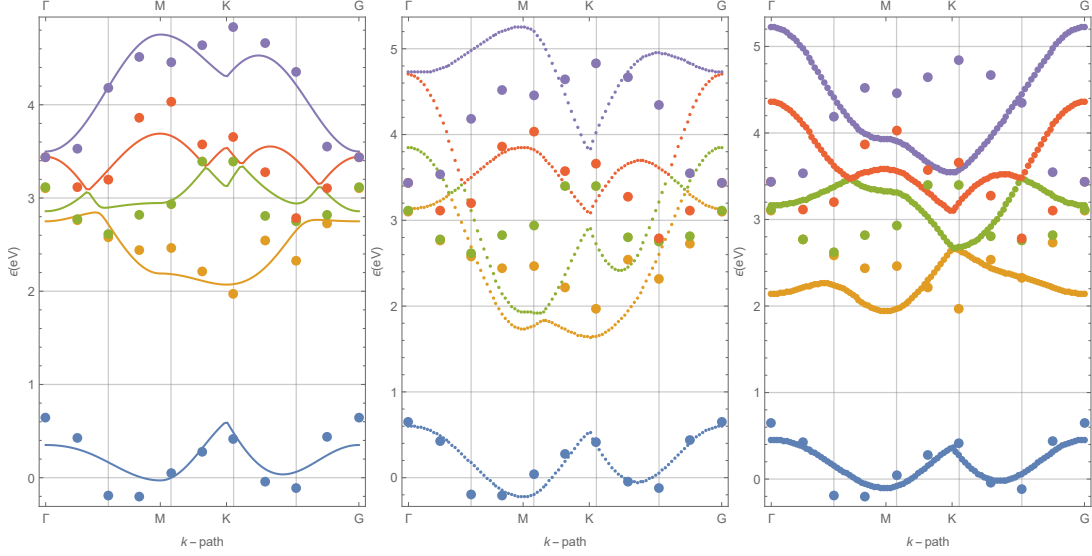


Figure 3: (Left) orthogonal fit with random initial parameter values between -1 and 1 eV, big dots represent DFT data while lines represent fit result. (Middle) Feed of orthogonal result output to nonorthogonal case initial input, big dots represent DFT data while small dots represent fit result. (Right) Nonorthogonal fit result with random initial values between -1 and 1 eV, big dots represent DFT data while medium dots represent fit result

| | | Time (s) | Residue (eV) ² |
|-------------------------|---|----------|---------------------------|
| Nearest Neighbours | Orthornogal fit | 6.6875 | 2.72498 |
| | orthogonal fit feed to Non-orthogonal fit | 34.1875 | 2.0854 |
| | Non-orthogonal fit | 62.2813 | 2.08086 |
| Next Nearest Neighbours | Orthornogal fit | 18.9219 | 4.21631 |
| | orthogonal fit feed to Non-orthogonal fit | 145.703 | 1.83953 |
| | Non-orthogonal fit | 181.219 | 1.62531 |

Table 1: Comparison of computation times with residue function values

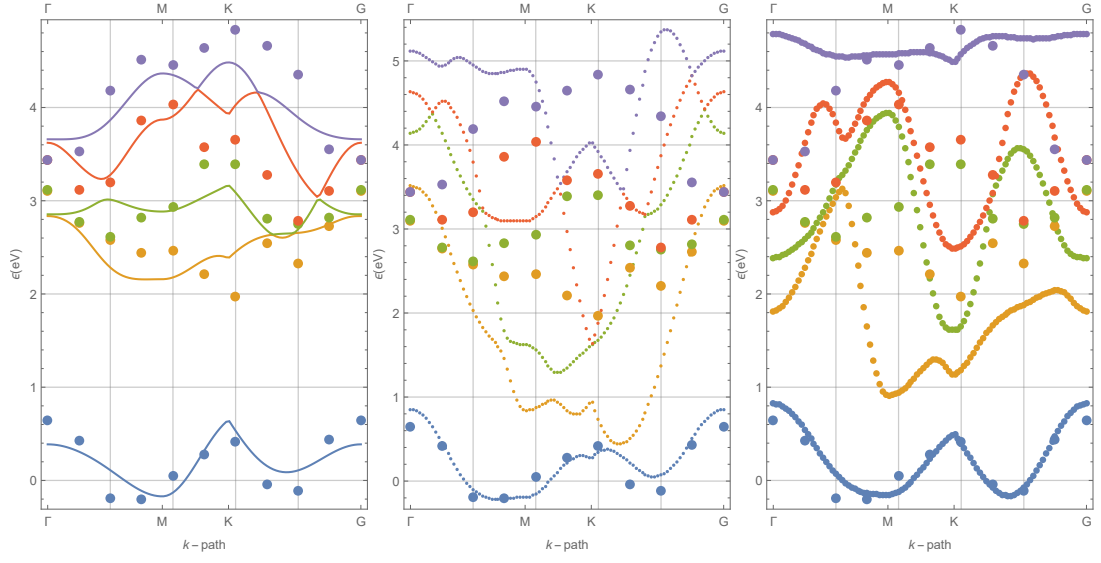


Figure 4: Same structure as Figure 3. (Left) orthogonal fit with random initial parameter values between -1 and 1 eV, big dots represent DFT data while lines represent fit result. (Middle) Feed of orthogonal result output to nonorthogonal case initial input, big dots represent DFT data while small dots represent fit result. (Right) Nonorthogonal fit result with random initial values between -1 and 1 eV, big dots represent DFT data while medium dots represent fit result

number of iterations for different starting points, there seems to be even more difficulty finding the global minimum as some of the fits appear worse in the non-orthogonal scheme. Thus, we conclude that the making the orthogonal approximation does not degrade the results obtained in any appreciable way.

Comparing the first and second set of calculations, it may also be seen that the increase in computation time once again is not proportionally justified by the increase in results accuracy. Even if we dismiss the non-orthogonal calculations as we have concluded that we will make the orthogonal approximation, the 83% increase in computation time is not matched by the 55% improvement in the residue function.

Hence, with the orthogonal and nearest-neighbour approximations, we proceed to perform more detailed computations in search of the best fitting parameters with which to define our effective tight-binding hamiltonian.

2.2.2 Refinement of Results

Keeping in mind now that we are most interested in the conduction band for the second part of the project on charge density waves in metallic TMDs, we now perform a more detailed fit with the following details:

- The basis is extended to include the three highest p orbitals of the chalcogen atom.
- Hoppings are now effectively next between next nearest-neighbours, namely consisting of
 - Metal atom to nearest chalcogen atom hoppings and vice versa (nearest-neighbour)
 - Metal atom to nearest metal atom hoppings (next nearest-neighbour)
 - Chalcogen atom to nearest same-plane chalcogen atom hoppings (next nearest-neighbour)
 - Hoppings between top and bottom chalcogen planes, for chalcogen atoms directly above and below one another on the z axis
- The fitting is performed to just three of the eleven bands (i.e 0 weightage to the 8 bands not fitted to), the conduction band and one band above and below it in hopes of ensuring no nearby bands cross the conduction band
- Different weights are assigned to each band for the fit
 - The top and bottom bands are assigned a base weightage of 1
 - The conduction band is given triple the base weight, 3.
- A uniform mesh of 50 k-points along the $\Gamma - M - K - \Gamma$ path are used in the fit
- A mesh of double this density is added in the regions about the Γ and K points as well as the local minimum in the conduction band between the Γ and K points

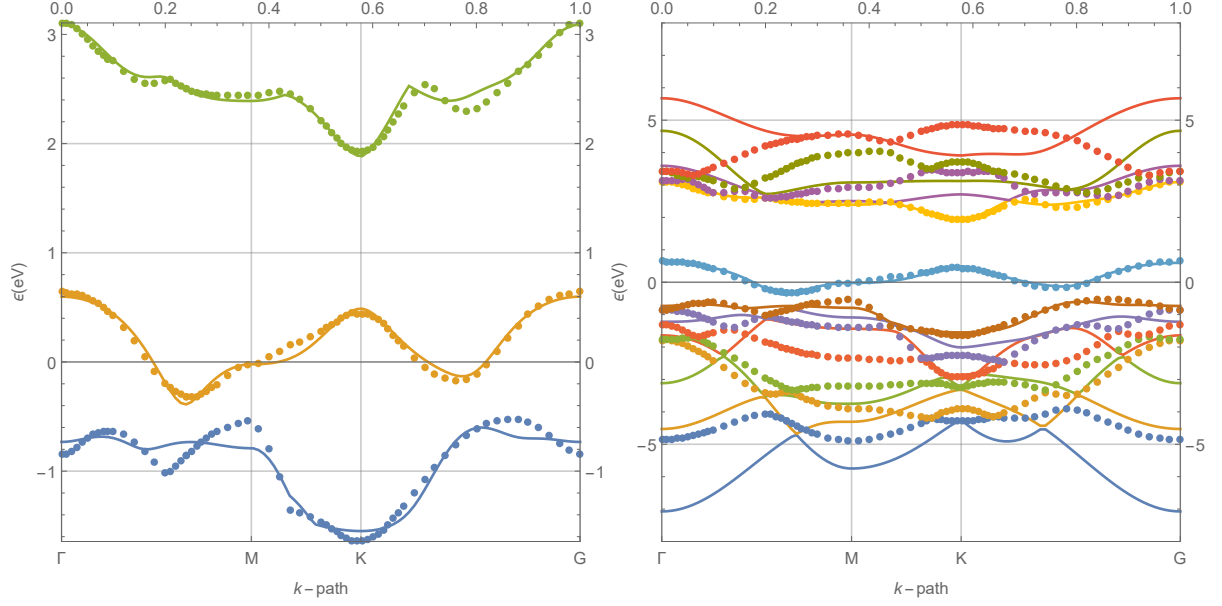


Figure 5: (Left) Tight-binding fitting results for three fitted bands. (Right) Tight-binding fitting results. Full eleven bands shown. Dots represent sampled DFT data, lines represent fitted data.

- A total of 1000 random starting points were used and that with the lowest residue is used in this report

The results are shown in Fig. 5 with the parameter values shown in Table 2. To aid in seeing how well the features of the conduction band were captured, we may also look at the full energy contour plot in 2-D k-space in Fig. 6.

As seen from the results, while the fit is hardly perfect, it demonstrates the useability of the code as an efficient alternative for generating tight-binding hamiltonians. If desired, a higher accuracy result can easily be obtained by adding more orbitals and neighbours into consideration or increasing sampling points. Similarly, if a quicker computation time is needed, one need only reduce any of the aforementioned quantities. For the purpose of the second part of this project, we take this existing result as it is and proceed to use it for our second objective, the charge density waves in metallic TMDs.

3 Charge Density Waves in metallic TMDs: Case Study of NbSe₂

3.1 Theoretical Background II:

3.1.1 Charge Density Waves (CDW)

To picture a CDW, one may first consider, in the simplest case, a one dimensional chain of metal atoms, equally spaced at a lattice constant a . The uniform distribution of

| | |
|---|---|
| $\epsilon_{d_{x^2y^2}} \rightarrow -0.352792$ | $V_{dd\pi}(a) \rightarrow -0.169265$ |
| $\epsilon_{d_{xy}} \rightarrow -1.76781$ | $V_{dd\sigma}(a) \rightarrow -0.907266$ |
| $\epsilon_{d_{yz}} \rightarrow 1.89222$ | $V_{pd\pi}(c) \rightarrow -1.27807$ |
| $\epsilon_{d_{z^2}} \rightarrow -1.65686$ | $V_{pd\sigma}(c) \rightarrow -0.654899$ |
| $\epsilon_{d_{zx}} \rightarrow 1.97177$ | $V_{pp\pi}(a) \rightarrow 0.0230759$ |
| $\epsilon_{p_x} \rightarrow -0.55683$ | $V_{pp\pi}(b) \rightarrow 1.99376$ |
| $\epsilon_{p_y} \rightarrow 0.444884$ | $V_{pp\sigma}(a) \rightarrow 1.03891$ |
| $\epsilon_{p_z} \rightarrow -1.74642$ | $V_{pp\sigma}(b) \rightarrow 0.875381$ |
| $V_{dd\delta}(a) \rightarrow -0.216206$ | |

Table 2: Tight-binding fitted parameters. a is the lattice constant. b is the distance from an Nb atom to the nearest Se atom. c is the distance between the top and bottom layers of Se atoms.

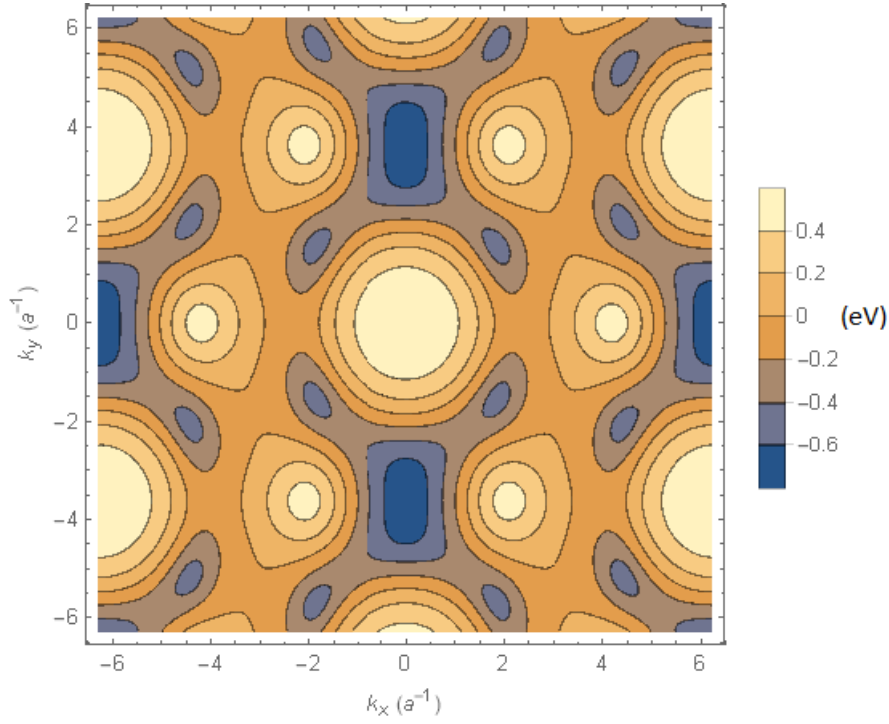


Figure 6: Fermi contour plot in k_x - k_y plane.

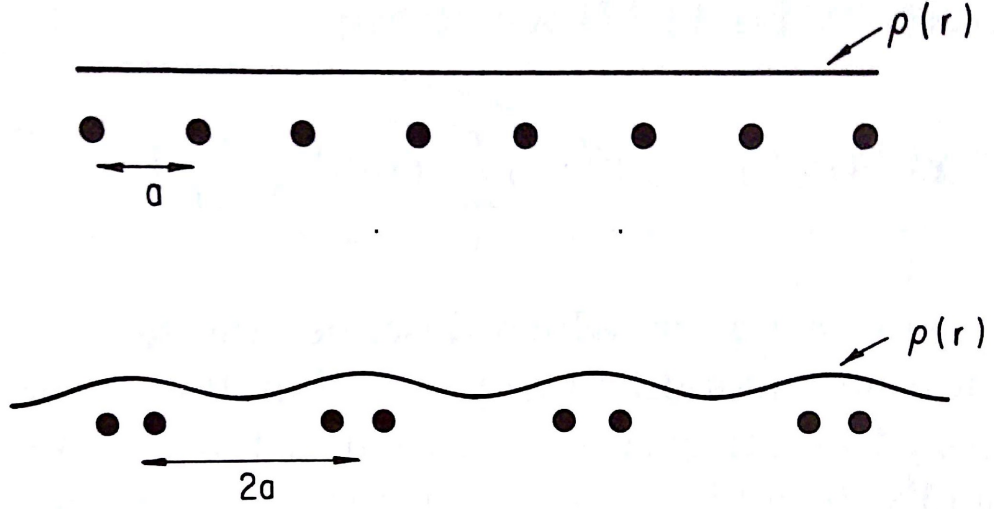


Figure 7: One possible formation of CDW by periodic distortion with period $2a$ of 1D chain of ions with lattice constant a . Reproduced from [3].

metal ions would imply a uniform distribution of charge formed by the electrons in the conduction band spread across the chain of ions to minimize total energy of the system. However, in the event that such a uniform chain is distorted, some regions in the chain will be less dense with ions than others, causing a comparative absence of electrons as electrons are attracted to regions of higher potential formed by the higher density of ions. If such a distortion is periodic in the lattice, the result will be a periodic distribution of the electron charge density matching the periodicity of the distribution of ions, thus forming what is known as a charge density wave. A simple illustration is shown in Fig. 7.

One account of the possible mechanism causing such a distortion in the first place may be explained as follows[3].

The hamiltonain describing electron and phonon states in a system can be written in second quantization form as:

$$H = H_{el} + H_{ph} = \sum_k \epsilon_k a_k^\dagger a_k + \sum_q \hbar \omega_q b_q^\dagger b_q$$

where a^\dagger , a and b^\dagger , b are the creation and destruction operators for electron and phonon states respectively. The equation of motion of the lattice ions then takes the form

$$\ddot{Q}_q = -\omega_q^2 Q_q$$

where Q_q are the normal coordinates. This equation leads to the usual phonon dispersion relation. If one considers the electron-phonon interactions, the hamiltonian is modified to

$$H = H_{el} + H_{ph} + H_{el-ph} = \sum_k \epsilon_k a_k^\dagger a_k + \sum_q \hbar \omega_q b_q^\dagger b_q + \sum_{k,q} g_{k,k+q} a_{k+q}^\dagger a_k (b_{-q}^\dagger + b_q)$$

where $g_{k,k+q}$ is the electron-phonon coupling coefficient. The k indices label the electron wavevector states while the q indices label the phonon wavevector states. The equation of motion would then become

$$\ddot{Q}_q = -\omega_q^2 Q_q - g \left(\frac{2\omega_q}{M\hbar} \right)^{1/2} \rho_q$$

where $\rho_q = \sum_k a_{k+q}^\dagger a_k$ is the fourier component of the electronic density. g was assumed first to be a constant, independent of q . This eventually leads to a renormalized phonon frequency given by

$$\Omega^2(q) = \omega^2(q) + 2\omega(q) |g|^2 \chi(q) \quad (5)$$

Where $\Omega(k)$ is the renormalized phonon frequency after perturbation and $\chi(q)$ is the Lindhard response function, given by

$$\chi(q) = \int \frac{f_k - f_{k+q}}{\epsilon_k - \epsilon_{k+q}} dk$$

f_k is the fermi distribution function and ϵ_k are the electronic energy states.

In general, $\chi(q)$ takes a negative value so the renormalized phonon frequency will decrease as a function of q . Specifically, things get more interesting when the renormalized frequency dips sharply at certain values of q . This process is often termed phonon softening in view of how a 'softer' spring has a lower frequency. Taking it one step further, if the frequency drops all the way to zero at a particular value of q , say q_{CDW} , the result is a static phonon of finite wavevector q_{CDW} . This is illustrated in Fig. 8. In other words, the displacement amplitude of the ions due to that phonon is fixed in time. The result is thus a periodic distortion of ions and hence charge density with wavevector q_{CDW} .

What is left then is to identify the cause of the phonon softening. Looking back at Eq. (5), we see that there are two possible sources. One from the Lindhard response function and the other, dropping the assumption that it is a constant w.r.t q , from the electron-phonon coupling coefficient $g(q)$. We shall now discuss the physical mechanisms governing these two factors.

As stated in the introduction, the target we are interested in for this project is the electron-phonon coupling matrix. Thus, in section 3.1.2, the discussion of the Lindhard response function will be brief. In section 3.1.3, experimental findings reported in a separate paper[10] will motivate our focus on the EPC matrix, followed finally by a more detailed discussion of the EPC matrix in section 3.1.4.

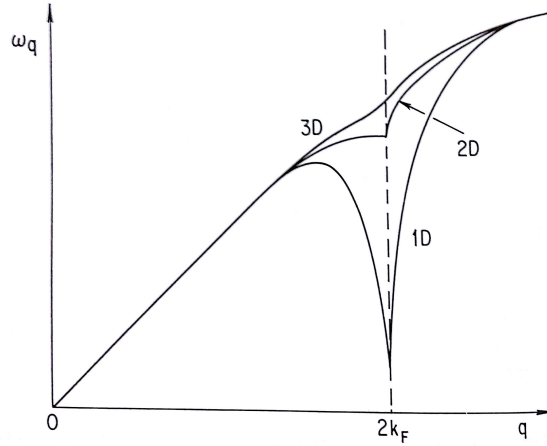


Figure 8: Phonon-softening due to divergence of $\chi(q)$ at q_{CDW} . Reproduced from [3].

3.1.2 Lindhard response function and Fermi Surface Nesting (FSN)

Historically, the idea of a charge density wave originates from Peierls who described the fundamental instability of a one-dimensional periodic chain of equally spaced atoms. He attributes the cause of this instability to what is known today as Fermi Surface Nesting (FSN). Briefly speaking, FSN occurs when there are a large number of pairs of filled and unfilled states on the fermi surface that are separated in k-space by the same vector. One example is shown in Fig. for a quasi-1D electron gas. We can first label that vector q_{CDW} as this difference in wavevector will be shown to correspond to the CDW wavevector. This allows for a phonon of wavevector q_{CDW} to scatter the electrons from the filled to the unfilled states elastically (since all points on the fermi surface by definition have the same energy ϵ_F).

Looking back at the Lindhard response function, one can see that the function peaks as the denominator tends to 0 when $\epsilon_k = \epsilon_{k+q}$. As the function is integrated over k , the more values of k the equality holds for, the greater the peak of the function. This condition is precisely fulfilled by FSN. When a large number of points with energy ϵ_F on the fermi surface are separated by the same vector q_{CDW} in k-space, we see that $\epsilon_k - \epsilon_{k+q_{CDW}} = 0$ for these large number of k-points, resulting in a peak in the Lindhard response function at $q = q_{CDW}$. This extremum of the function at a particular value of q is exactly the trend we are looking for in formation of charge density waves.

3.1.3 Experimental findings for NbSe₂. FSN vs EPC

In a paper by Zhu et al [10], they present a compilation of published experimental data on NbSe₂ and an analysis on how the evidence point toward EPC as the driving force behind the CDW phase in NbSe₂ and not FSN. I summarize some of their key findings here to illustrate our motivation for attempting to compute the EPC matrix for NbSe₂.

The CDW phase in NbSe₂ is known [2, 6, 10] to occur with $q_{CDW} \simeq \frac{2}{3}|\Gamma M| = 0.695\text{\AA}^{-1}$

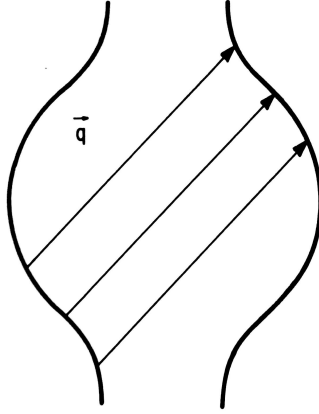


Figure 9: Fermi surface of a quasi 1-D electron gas and nesting vectors q . Reproduced from [3].

at $T = 33.5K$. $|\Gamma M|$ denotes the length of the $\Gamma - M$ path in the first brillouin zone of the undistorted NbSe₂ lattice. Fig. 10 shows a fermi surface plot computed from a tight-binding fit to angle-resolved photoemission spectroscopy(ARPES) data as well as the CDW wavevector q_{CDW} obtained from diffraction measurements for NbSe₂. A quick glance already casts doubt that FSN is at work in this particular system. To be more certain, we continue to look at the numerical plots. Fig. 11 shows experimentally obtained data about the phonon energy dispersion and plots of the real and imaginary parts of the the Lindhard response function along the $\Gamma - M$ high symmetry path in the brillouin zone. The sharp phonon energy dip at q_{CDW} thus indicates where we should expect to find peaks in either the EPC matrix or the Lindhard response function. If FSN was indeed the driving mechanism, one would expect a peak in the function at q_{CDW} . Evidently, however, there is no compelling sign of the function peaking at q_{CDW} . In an effort to see then if EPC is really the driving force of the CDW phase transition here, $|g(q)|^2$ is fitted to the phonon linewidth data using the relation

$$L_{EPC}(q) = -2|g(q)|^2 \text{Im}[\chi(q)]$$

where $L_{EPC}(q)$ is the phonon linewidth. Fig. 12 shows the plot of $|g(q)|^2$ and the renormalized phonon energy dispersion as calculated from the values of $|g(q)|^2$. Although there might be a natural correlation between the phonon softening and $|g(q)|^2$ found in this manner, it would still seem that it is the more likely driver of the CDW phase since based on the lack of a convincing peak in $\chi(q)$. Based on these arguments, we have decided to focus efforts on calculating $|g(q)|^2$ using our tight-binding model.

3.1.4 Electron-Phonon Coupling (EPC)

The electron-phonon coupling matrix characterises the interaction of electrons with phonons in a system. This is done by studying how electrons are scattered from one

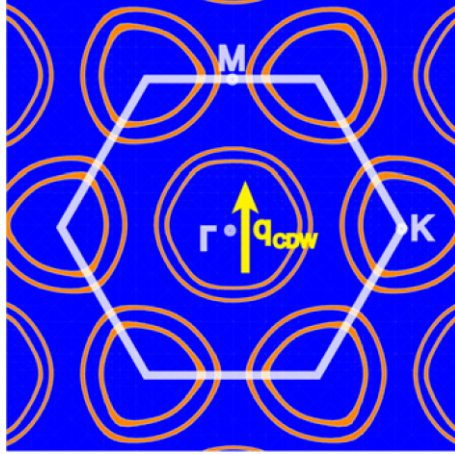


Figure 10: Fermi surface plot and q_{CDW} of NbSe₂. Reproduced from [10].

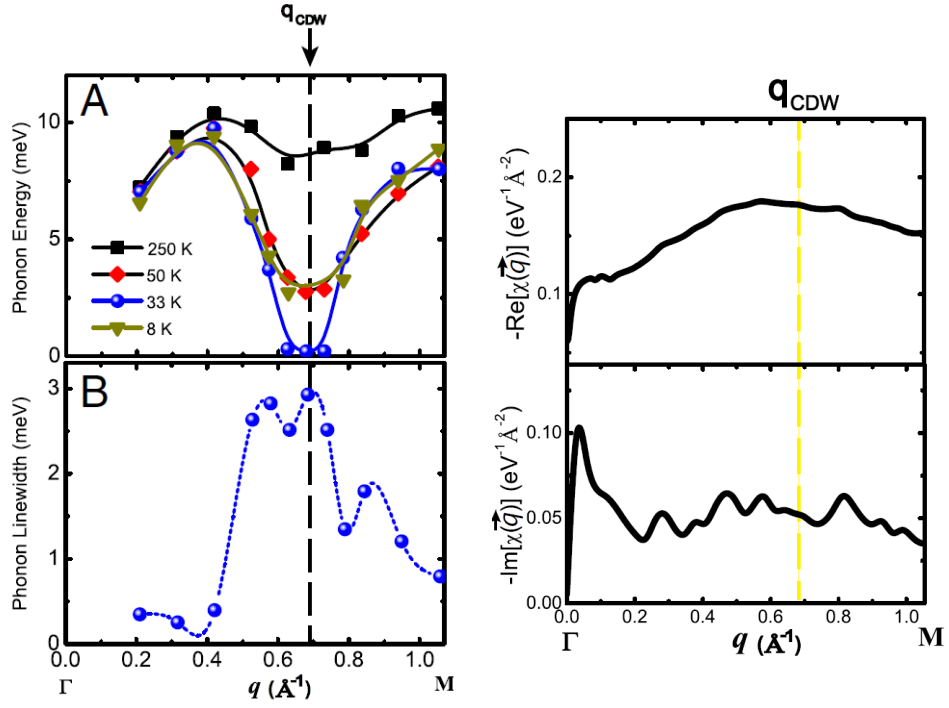


Figure 11: (Left) Experiment measurements of phonon energy dispersion along the $\Gamma - M$ high symmetry path computed phonon-linewidth from measured bandstructure. (Right) Real and Imaginary parts of $\chi(q)$ calculated from experimental data, plotted along $\Gamma - M$ direction. Reproduced from [10].

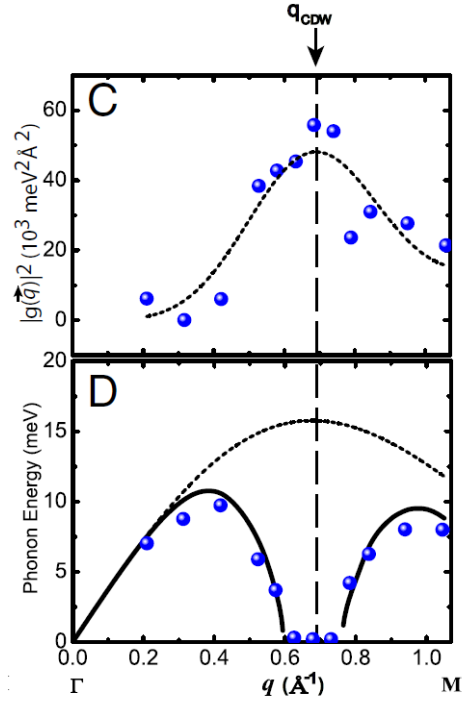


Figure 12: (C) $|g(q)|^2$ obtained from fitting to phonon linewidth data. (D) Phonon energy dispersion calculated from $|g(q)|^2$. Reproduced from [10].

state to another when encountering a phonon. The strategy employed, by Varma et al[8], is to treat the phonons as perturbative lattice distortions and study the resultant perturbation to the electron hamiltonian. The following is a quick summary of the key features in the derivation, rewritten to match the notation used earlier in our tight-binding scheme, as well as omitting all orbital overlap \mathbf{S} matrices as we have used the orthogonal tight-binding scheme.

We may start with the form of the LCAO state constructed earlier in Eq. (3), but note that the following states are not the same states, but instead the time-perturbed solutions. We thus notate them differently, as the unperturbed terms will enter into these equations eventually.

In the most general case, given explicit time dependence, both the coefficient as well as the basis states can depend on time:

$$\Phi(t) = \sum_{nk} c_{nk}(t) \psi_{nk}(t)$$

Now in the presence of perturbation, the hamiltonian will in general be modified and can be written as $H' = H + \delta H$ where H represents the unperturbed hamiltonian and δH is the change due to perturbation. The equation of motion for the perturbed system may be given by

$$i\dot{\Phi} = H'\Phi$$

Solving for this approximately gives

$$i\dot{c}_{nk} \simeq \sum_{\alpha i, \beta j} ([b_{\alpha i}^n(k)]^\dagger \delta H_{\alpha i, \beta j}(k) [b_{\beta j}^{n'}(k')]) c_{n'k'} \quad (6)$$

where $b_{\alpha i}^n(k)$ is the eigenvector as defined in Eq. (4), $H_{\alpha i, \beta j}$ here represents the use of the tight-binding matrix form of the hamiltonian.

The equations thus far have been for general perturbations. Next is to specify the type of perturbation by defining δH . For electron-phonon coupling, Varma defines it as

$$\delta H_{\mu\alpha i, \nu\beta j}^\sigma = \nabla_{\mu-\nu, \sigma} H_{\mu\alpha i, \nu\beta j} \cdot (\vec{u}_\mu - \vec{u}_\nu)$$

where μ and ν index lattice sites and \vec{u}_μ is the displacement of lattice site μ from the unperturbed equilibrium position. σ indexes a cartesian coordinate in k-space. δH is thus expressed as the change in hamiltonian due to the change in distance between lattice sites due to the phonon distortions. In terms of the normal coordinates $u_{\mu\sigma} = \sum_{q, \zeta} \eta_{q\zeta}^\sigma e^{iq \cdot R} i u_{q\zeta}$, where ζ is the polarization and $\eta_{q\zeta}^\sigma$ is the matrix element in the σ cartesian direction of the corresponding polarization vector, Eq. (6) then becomes

$$i\dot{c}_{nk} \simeq \eta_{k-k', \zeta}^\sigma g_{kn, k'n'}^\sigma c_{n'k'} u_{k-k', \zeta}$$

where

$$g_{kn, k'n'}^\sigma = \sum_{\alpha i, \beta j} (b_{kn}^\dagger \sum_{\mu\nu} [\nabla_\sigma H_{\alpha i, \beta j}(k) \times e^{ik \cdot R_{\mu\nu}} - \nabla_\sigma H_{\alpha i, \beta j}(k') \times e^{ik' \cdot R_{\mu\nu}}] b_{k'n'})$$

Considering the quickly decaying hopping overlaps of a tightly-bound system, a final approximation can be made to give

$$g_{kn,k'n'}^\sigma = \lambda^2 [b_{kn}^\dagger (\nabla_\sigma H_k - \nabla_\sigma H_{k'}) b_{k'n'}] \quad (7)$$

Here, λ^2 is the product of the lattice constant and the logarithmic derivation of the tight-binding matrix element with distance. α indexes the cartesian direction in k-space, and μ indexes the energy band we are looking at. $\nabla_\alpha H_k$ is then simply the derivative of the hamiltonian at state k in the k_α and b_{kn} are the same eigenvectors as in Eq. 4 just with the index n written as a subscript instead

3.2 Computation of the EPC matrix $g_{kn,k'n'}^\sigma$

With Eq. (7), by omitting λ^2 in our calculations as it is effectively just a scaling constant, we may easily compute the EPC matrix $g_{kn,k'n'}^\sigma$ using the obtained tight-binding hamiltonian matrix. In this case, we are interested in finding the matrix components corresponding to scatterings between energy levels within the conduction band, in the k-space direction corresponding to $k - k'$ i.e. the longitudinal acoustic phonon mode, believed to be the primary source of the CDW instability[6]. We denote this specifically by $g_{k,k+q}^l$, dropping the band index n and rewriting k' as $k + q$ since we know $q = k' - k$ by conservation of momentum. We may first plot its absolute value along k-space. In the most general case, the value depends on the initial state k , not just the vector $k - k'$ connecting the two states. This is indeed observed in our results as the plots vary considerably depending on the initial state k . This is shown in Fig. 13 where each band represents a different initial state k along the $\Gamma - M$ high symmetry path, scattered to the final state k' also along the $\Gamma - M$ path (as this is where q_{CDW} is expected to occur as seen from the data in section 3.1.3). This renders the assumptions of constant g made in Gruner's derivation of the renormalized frequency[3] as well as that $g(q)$ only depends on the difference difference in wavevector $k - k'$ in the work of Zhu et al[10] invalid in this project. To account for this, one would have to integrate $|g_{k,k+q}^l|^2$ over the different values of k . As an approximation, we replace the integral with a discrete sum and restrict the values of k to the vicinity of the fermi level. This is done by sampling a k-mesh with k_x and k_y going from -2π to 2π in steps of 0.1 and picking points corresponding to fermi energy within $\pm 0.01\text{eV}$ of the fermi energy. We consider this to be the most important region firstly because using a DFT 0 temperature result, we expect majority of the interactions to occur on or near the fermi surface. This can be understood with the following illustration.

At $T = 0$, all the electron levels will be filled up to the fermi energy. If an electron is scattered by a phonon, by Pauli's Exclusion Principle, it can only scatter to an unoccupied state at or above the fermi level, depending on whether or not it was partially or fully filled. By conservation of energy, the result is an electron deeper in the shell will require a phonon of higher energy to be scattered. Thus, it is a higher probability of phonons with enough energy to scatter electrons near the fermi surface than those deeper in the shell.

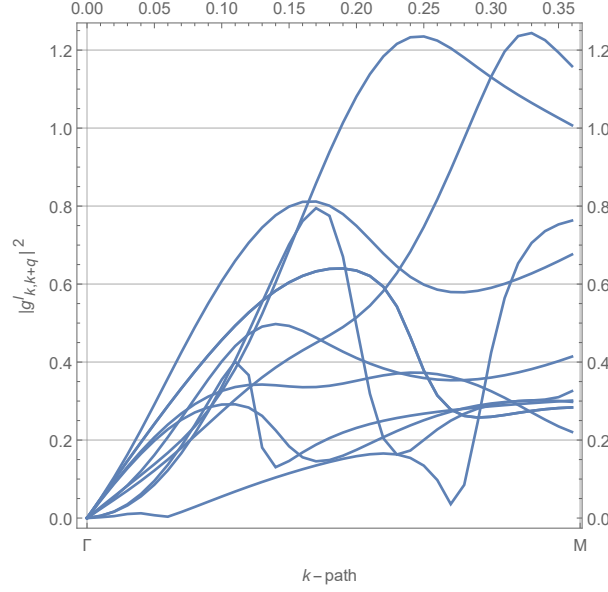


Figure 13: Plots of $|g_{k,k+q}^l|^2$ along the $\Gamma - M$ high symmetry path

Another reason for the emphasis on states near the fermi energy is because the phonon renormalization depends also on $\chi(q)$. A peak in $|g_{k,k+q}^l|^2$ can always be offset by a particularly small value of $\chi(q)$. At $T = 0$, the fermi distributions are either 1 or 0 depending on whether the state is filled or not. This firstly has the same result as Pauli's Exclusion Principle of scatterings being only possible between a filled state and an unfilled state, otherwise leading to a numerator of 0 in $\chi(q)$. Secondly, looking at the denominator, an overly large energy difference between the states would also dampen $\chi(q)$ and offset the peak in $|g_{k,k+q}^l|^2$. Thus, the smallest energy differences between filled and unfilled states would correspond to those within the vicinity of the fermi surface.

The result obtained from the average of $|g_{k,k+q}^l|^2$ over the fermi surface is thus shown in Fig. 14.

From Fig. 14, we do see a very approximate appearance of a peak along the $\Gamma - M$ path although it somewhat misses the $\frac{2}{3}$ mark with a discrepancy of 19%. Looking back at our calculations, there are a number of sources of this sizeable error.

At the very root of the calculations is the tight-binding band hamiltonian we have adopted. Aside from the slight mismatch present in every imperfect fit, we note that particularly at the fermi level crossings, there are considerable differences. This is likely a cause for the deformed fermi surface we have obtained as a result as seen in Fig. 6. Its shape is visibly already different from that seen in the work of Zhu et al shown earlier in Fig. [10]. Even without making that comparison, there is a clear lack of the hexagonal symmetry expected from the reciprocal lattice structure. Considering how our calculations were based on the regions near the fermi surface, a significantly

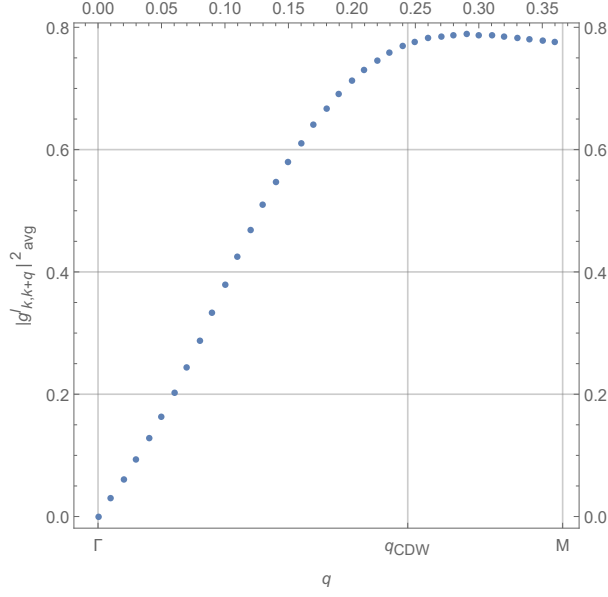


Figure 14: Mean of $|g_{k,k+q}^l|^2$ within $\pm 0.01 \text{ eV}$ of the Fermi surface

distorted Fermi surface would naturally add a significant distortion to the result. To see this quantified, we tried raising the Fermi level artificially by sampling points about 0.4 eV instead of 0 eV leading to the result shown in Fig. 15. In this case, the result is greatly improved with a discrepancy of just 6%. The maximum point is also sharper and more well-defined.

For future considerations, noting that the quality of our results is limited by the quality of our reference energy bands used for the tight-binding fit, it is good to ensure that the physical features important to us are described adequately by performing preliminary calculations using the reference energy bands themselves, a check that was not performed for this project. This will ensure that the target level of accuracy is readily attainable if the tight-binding model is refined well enough. With regards to the fitting procedure, more could have been done to pay attention to the Fermi level crossing by increasing the density of sampling points such as was done with the turning points and the Γ and K points.

4 Conclusion

In conclusion, the automation of the tight-binding Hamiltonian performs up to expectations, allowing for easy reconstruction using different lattice structures in a clear and straightforward manner. The fitting of parameters can also be tuned accordingly depending on areas of importance for different types of materials and overall levels of accuracy desired for a given calculation. This is of particular importance in tight-binding as its effectiveness as a semi-empirical method is largely due to its ability to balance accuracy

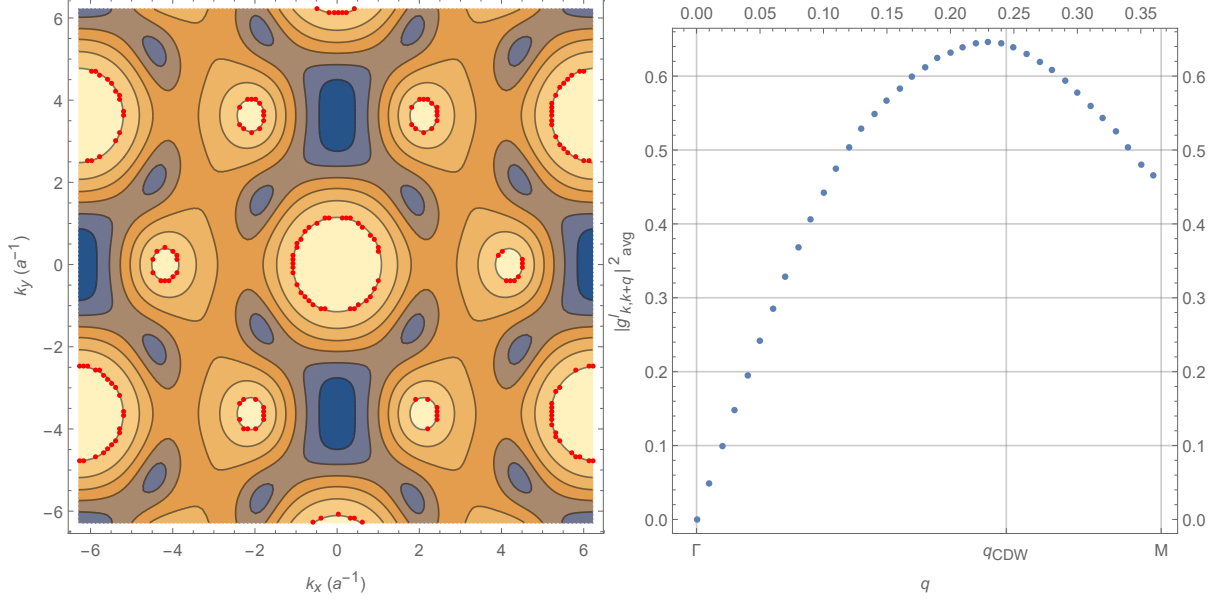


Figure 15: (Left) New sampling region marked by red dots on conduction band energy contour. (Right) Mean of $\left|g_{k,k+q}^l\right|^2$ within $\pm 0.01\text{eV}$ of 0.4eV

of results with simplicity of the hamiltonian. The balance point can vary largely for different calculations and different purposes, making quick and easy tuneability of this aspect key to being able to find a hamiltonian with just the right amount of accuracy and simplicity for a particular purpose. The main bottleneck in efficiency occurs in computation time in performing the fit which is largely unavoidable for a large basis with many fitting parameters. As for the electron-phonon coupling matrix, it would seem unfortunate that the distortion of the fermi-surface in our tight-binding solution might have been the biggest hurdle in preventing the correlation between electron-phonon coupling and charge density waves in NbSe₂. Nevertheless, future calculations can be readily done with the tight-binding code already in place and calculation procedures well laid out. As mentioned, improvements could be made to fitting near the fermi energy, or other more accurate bandstructure data can be found and used as a reference. Additionally, restrictions were not placed on the values of the fitting parameters based on physical intuition such as knowledge of relative on-site energies based on crystal field splitting. These could further be added in to improve accuracy of results in future calculations.

References

- [1] Chhowalla, M., Shin, H. S., Eda, G., Li, L., Loh, K. P., & Zhang, H. (2013). The chemistry of two-dimensional layered transition metal dichalcogenide nanosheets. *Nature Chemistry*, 5(4), 263-275. doi:10.1038/nchem.1589
- [2] Ge, Y., & Liu, A. Y. (2012). Effect of dimensionality and spin-orbit coupling on charge-density-wave transition in 2H-TaSe₂. *Physical Review B*, 86(10) doi:10.1103/PhysRevB.86.104101
- [3] Gruner, G. (1994). *Density waves in solids*. Reading, Mass: Addison-Wesley Pub. Co., Advanced Book Program.
- [4] Jariwala, D., Sangwan, V. K., Lauhon, L. J., Marks, T. J., & Hersam, M. C. (2014). Emerging device applications for semiconducting two-dimensional transition metal dichalcogenides. *ACS Nano*, 8(2), 1102.
- [5] Kumar, A., & Ahluwalia, P. K. (2013). Effect of quantum confinement on electronic and dielectric properties of niobium dichalcogenides NbX₂ (X=S, se, te). *Journal of Alloys and Compounds*, 550, 283-291. doi:10.1016/j.jallcom.2012.09.068
- [6] Moncton, D. E., Axe, J. D., & DiSalvo, F. J. (1977). Neutron scattering study of the charge-density wave transitions in 2H-TaSe₂ and 2H-NbSe₂. *Physical Review B*, 16(2), 801-819. doi:10.1103/PhysRevB.16.801
- [7] Slater, J. C., Koster, G. F. Simplified LCAO method for the periodic potential problem. *Phys. Rev.* 94, 1498 (1954).
- [8] Varma, C. M., Blount, E. I., Vashishta, P., & Weber, W. (1979). Electron-phonon interactions in transition metals. *Physical Review B*, 19(12), 6130-6141. doi:10.1103/PhysRevB.19.6130
- [9] Wang, Q. H., Kalantar-zadeh, K., Kis, A., Coleman, J. N., & Strano, M. S. (2012). Electronics and optoelectronics of two-dimensional transition metal dichalcogenides. *Nature Nanotechnology*, 7(11), 699. doi:10.1038/nnano.2012.193
- [10] Zhu, X., Cao, Y., Zhang, J., Plummer, E. W., & Guo, J. (2015). Classification of charge density waves based on their nature. *Proceedings of the National Academy of Sciences*, 112(8), 2367-2371. doi:10.1073/pnas.1424791112